

Emergence of Climate Change in the Tropical Pacific

Jun Ying (yingjun@sio.org.cn)

Second Institute of Oceanography, Ministry of Natural Resources https://orcid.org/0000-0002-4725-9517

Matthew Collins

University of Exeter https://orcid.org/0000-0003-3785-6008

Wenju Cai

CSIRO Oceans and Atmosphere https://orcid.org/0000-0001-6520-0829

Axel Timmermann

Center for Climate Physics, Institute for Basic Science

Ping Huang

Institute of Atmospheric Physics https://orcid.org/0000-0001-7891-8848

Dake Chen

Lamont-Doherty Earth Observatory

Karl Stein

Center for Climate Physics, Institute for Basic Science

Article

Keywords: climate change, tropical Pacific, time of emergence, El Niño-Southern Oscillation

Posted Date: September 3rd, 2021

DOI: https://doi.org/10.21203/rs.3.rs-842462/v1

License: © 1 This work is licensed under a Creative Commons Attribution 4.0 International License.

Read Full License

Version of Record: A version of this preprint was published at Nature Climate Change on March 7th, 2022. See the published version at https://doi.org/10.1038/s41558-022-01301-z.

Emergence of Climate Change in the Tropical Pacific

- 2 Jun Ying^{1,2,3*}, Matthew Collins³, Wenju Cai^{4,5,6}, Axel Timmermann^{7,8}, Ping Huang^{9,10},
- 3 Dake Chen^{1,2,11}, and Karl Stein^{7,8}
- 4 1. State Key Laboratory of Satellite Ocean Environment Dynamics, Second Institute
- of Oceanography, Ministry of Natural Resources, Hangzhou, 310012, China
- 6 2. Southern Marine Science and Engineering Guangdong Laboratory (Zhuhai),
- 7 Zhuhai, China
- 8 3. College of Engineering, Mathematics and Physical Sciences, University of Exeter,
- 9 Exeter, United Kingdom
- 10 4. Frontier Science Centre for Deep Ocean Multispheres and Earth System and
- 11 Physical Oceanography 9 Laboratory, Ocean University of China, Qingdao, China.
- 12 5. Qingdao National Laboratory for Marine Science and Technology, Qingdao, China.
- 13 6. Centre for Southern Hemisphere Oceans Research (CSHOR), CSIRO Oceans and
- 14 Atmosphere, Hobart 12 7004, Australia.
- 15 7. Center for Climate Physics, Institute for Basic Science (IBS), Busan, South Korea.
- 16 8. Pusan National University, Busan, South Korea.
- 9. Center for Monsoon System Research, Institute of Atmospheric Physics, Chinese
- 18 Academy of Sciences, Beijing 100190, China
- 19 10. State Key Laboratory of Numerical Modeling for Atmospheric Sciences and

- 20 Geophysical Fluid Dynamics, Institute of Atmospheric Physics, Chinese Academy
- of Sciences, Beijing, 100190, China
- 22 11. School of Oceanography, Shanghai Jiao Tong University, Shanghai, China
- *Corresponding to: yingjun@sio.org.cn

Abstract

25

26

27

28

29

30

31

32

33

34

35

36

37

38

39

Future changes in both the mean climate of the tropical Pacific and characteristics of the El Niño-Southern Oscillation (ENSO) are now established as being likely. Determining the time of emergence (ToE) of detectable climate change signals against background noise of natural variability is critical to mitigation strategies and adaptation planning. Here, we find that the annual-mean SST signal, mainly reflecting the tropical-mean warming signal, has already emerged in the historical period across much of the tropical Pacific, with the latest ToE in the east. The annual-mean rainfall signal is expected to emerge by around mid-century based on the multi-model ensemble mean (MEM) result, with some sensitivity to emission scenarios. By contrast, the signal of ENSO-related rainfall variability is projected to emerge by around 2040±3 based on the MEM regardless of emission scenarios, ~ 30 years sooner than that of the ENSO-related SST variability. Our results are instructive for detection of climate change signals in the tropical Pacific and reinforce the severe risks of ENSO-induced climate extremes that are fast emerging regardless of any mitigation actions.

41

40

Main Text:

Hosting the El Niño–Southern Oscillation (ENSO), the world's largest source of interannual variability, the tropical Pacific plays a pivotal role in human-induced global climate change¹. How the tropical Pacific responds to rising anthropogenic greenhouse gases (GHGs) has been one of the most important issues of climate²-⁴. Projected SST changes from coupled general circulation models (CGCMs) display on average a faster eastern equatorial warming than surrounding regions, characterized by a weakened west-minus-east SST gradient⁴-₹. However, recent observations display an enhanced west-minus-east SST gradient and an eastern equatorial cooling, although the pattern of change is sensitive to SST reconstruction used and the period over which the trend is calculated^{8,9}. The tropical mean-state rainfall generally increases in regions where there is more SST warming than the tropical-mean—the so-called "warmer gets wetter" paradigm⁴.

On interannual timescales, the change in ENSO-related SST variability (hereafter ENSO SST) is projected as being likely^{7,10,11}, although large inter-model diversity exits¹²⁻¹⁶. While the change in ENSO-related rainfall variability (hereafter ENSO rainfall) is projected to increase with a robust inter-model consensus¹⁷⁻²², owing to increased mean-state moisture and faster warming in the eastern equatorial Pacific (EEP).

However, it remains unclear when these anthropogenic signal will emerge out of the large background noise of natural variability, and - to our knowledge - only one study has addressed the potential detectability of human-induced ENSO variance changes²³. The knowledge is fundamental for adaptation planning and risk assessment for affected regions. Here we use outputs of climate models participating in Coupled

Model Intercomparison Project Phase 6 (CMIP6) (ref. ²⁴) to determine the time of emergence (ToE) of the anthropogenic climate change signal in the tropical Pacific relative to the background noise in terms of tropical mean state change²¹ and ENSO SST and rainfall.

Time of Emergence of Mean SST and Rainfall Change Signals

67

68

69

70

71

72

73

74

75

76

77

78

79

80

81

82

83

84

85

86

87

88

89

90

We begin by investigating the ToE of annual-mean SST based on 23 CMIP6 models under historical forcing before 2014 and various shared socioeconomic pathway (SSP) emission scenarios thereafter (see "CMIP6 models, observed datasets, and processing" in Methods), which requires estimates of both signal and noise of annualmean SST. The annual-mean SST signal over the 1870 to 2099 period is calculated by regressing grid-point annual-mean SST change from the 1870–1899 reference period onto the time series of global warming SST change that is smoothed by fitting a fourth order polynomial (see "Signal, noise, and ToE of annual-mean SST and rainfall" in Methods). Map of multi-model ensemble mean (MEM) regression coefficients, representing the response of annual-mean SST to global warming, displays a basinwide warming in the tropical Pacific together with more warming in the EEP (Fig. 1a, shaded), consistent with previous studies based on CMIP3 (ref. ^{25,26}) or CMIP5 (ref. ^{5,27}) models. Background natural variability is taken as the noise for annual-mean SST change signal and represented by the interannual standard deviation of SST computed from 500-year-long experiments under a constant pre-industrial CO₂ level (piControl), Spatial pattern of the noise exhibits largest values in the EEP region due to ENSO variability (Fig. 1a, Contours).

The **ToE** of annual-mean SST, defined at each grid point as the first time the signal of SST change is greater than the noise²⁸, indicates that the climate change signal is

already detectable across the whole tropical Pacific, with the signal having emerged latest in the EEP (Fig. 1b; Supplementary Fig. 1). The distribution of the ToE and the noise have a similar pattern, with the spatial correlation up to 0.91 in MEM (Fig. 1b) and being all statistically significant in individual models (Supplementary Fig. 1), indicating a dominant role of the noise in shaping the spatial distribution of the ToE of annual-mean SST in models.

On the other hand, the MEM annual-mean rainfall response to global warming displays a robust increase along the central to eastern equatorial Pacific with a high inter-model consensus, and there is hardly any signal that has inter-model consistency on the flanks where the climatological Intertropical Convergence Zone (ITCZ) and South Pacific Convergence Zone (SPCZ) are located (Fig. 1c, shaded). The MEM noise of annual-mean rainfall exhibits a pattern with large values in the central equatorial Pacific, ITCZ and SPCZ regions, and a local minimum in the EEP (Fig. 1c, contours). The estimated MEM ToE in most models under the SSP585 scenario, indicates that the annual-mean rainfall signal can be expected to emerge within the coming decades in the EEP, although no emergent signal appears in the ITCZ and the SPCZ by the end of the 21st century (Fig. 1d).

We then focus on the EEP region where both detectable signals of annual-mean SST and rainfall emerge in most models (Fig. 1b, d). The ToE of EEP annual-mean value is defined as when the spatial-mean of grid-point signal-to-noise ratio is greater than 1.0 for the first time. As shown in Fig. 2a. the annual-mean SST signals, calculated based on the MEM under all the four emission scenarios, emerge at around the year 2000, sooner than the ToE in the three sets of SST observations. For individual models under the SSP585 scenario, 19 out of 23 models already have detectable annual-mean SST signals in the EEP before 2020, with signals emerging as early as the 1980s in a

few models (Fig. 2b). The spatial patterns of the ToE of the observed annual-mean SST show the signal emerging in parts of the tropical Pacific by 2019 but not, in general, in the EEP (Supplementary Fig. 2). The observed SST from COBEv2 shows the largest spatial coverage of emergence (Supplementary Fig. 2c) and indicates emergence of the signal averaged over the EEP (Fig. 2b). The differences in ToE of annual-mean SST among three observational datasets suggest that observational uncertainties play a role^{8,29}.

Given that the background noise (Fig. 2c) and smoothed global-mean SST change (Supplementary Fig. 3) between MEM results and observations are both comparable in magnitude, the model-observation discrepancy in the ToE of EEP annual-mean SST signal seems to be mainly attributable to different responses of local annual-mean SST to global warming (Fig. 2d). The responses of observed annual-mean SST, though with a similar basin-wide warming, display a pattern with an enhanced west-minus-east SST gradient featuring an EEP minimum warming (Supplementary Fig. 4a–c), in contrast to the local maximum warming in the MEM with a small inter-model difference (Fig. 1a, Fig. 2d).

We decompose the annual-mean SST into two components: the tropical-mean SST $(T_{\rm tm})$ and the relative SST $(T_{\rm r})$ that is the deviation from the tropical-mean⁴ (see "Decomposition of *annual-mean* SST and rainfall change" in Methods). By doing so, we find the model-observation difference in the EEP annual-mean SST response to global warming is caused by the difference in the response of local $T_{\rm r}$, rather than that of $T_{\rm tm}$ (Fig. 2d). In the MEM as well as individual models, the $T_{\rm r}$ shows a robust warming response in the EEP, whereas in observations there is consistent cooling response, albeit with different magnitudes (Fig. 2d, Supplementary Fig. 4d–g). Note

that 4 out of 23 models do not show a detectable signal in the EEP by the year 2020 (Fig. 2b), which could be due to stronger simulated background noise (Fig. 2c), rather than a weaker local response of annual-mean SST to global warming (Fig. 2d).

An inter-model relationship reveals that the ToE of the EEP annual-mean SST is highly correlated to the earlier ToE of the $T_{\rm tm}$ (r=0.89, Fig. 2e), but not to the much later ToE of the EEP $T_{\rm r}$, which emerges in only about half of the 23 models (Fig. 2f). Thus the modelled emergent signals of the EEP annual-mean SST mainly reflect signals of the $T_{\rm tm}$. The earlier ToE of the $T_{\rm tm}$ is a result of both a stronger response of the $T_{\rm tm}$ (Fig. 2d) and weaker background noise (Supplementary Fig. 5a), while the later ToE of the $T_{\rm r}$ is caused by both a weaker response of the $T_{\rm r}$ (Fig. 2d) and stronger background noise (Supplementary Fig. 5b).

Given comparable ToE of $T_{\rm tm}$ (Fig. 2e) and noise of $T_{\rm r}$ (Supplementary Fig. 5b) between the MEM results and observations, the model-observation discrepancy in the ToE of annual-mean SST is thus mainly due to the much-discussed difference between a warming response of $T_{\rm r}$ in the EEP featuring a weakened west-minus-east SST gradient in models and an opposite response in observations. Although cause for such opposite response is still a matter of debate^{30,31}, we find that both the modelled and observed responses of EEP $T_{\rm r}$ are dependent on the length of the time period over which the responses are computed. Regardless of whether the modelled EEP $T_{\rm r}$ response is warming or cooling in historical simulations, it can be warming in future projections when the time period is extended to the end of 21st century (Supplementary Fig. 6). Thus, a pattern with an EEP warming response of $T_{\rm r}$ featuring a weakened west-minus-east SST gradient should not be excluded in the future real world.

For rainfall in the EEP, we focus on the model outputs, as observational records are reliable only during the satellite era, thus too short to capture the long-term global warming-induced signal. The estimated MEM ToE under different emission scenarios shows that detectable signals of annual-mean rainfall can be found in around midcentury under the SSP245, SSP370 and SSP585 scenarios (in years 2059, 2047 and 2038, respectively), but not under the SSP126 scenario which features the lowest GHGs forcing (Fig. 3a). For individual models under the SSP585 scenario, all models show detectable signals of annual-mean rainfall by the end of 21st century, but 19 out of 23 models show them after 2020 (Fig. 3b), suggesting a robust inter-model consensus of the not yet detectable signal of annual-mean rainfall. The inter-model difference of ToE for annual-mean rainfall, with signals emerging as early as before 2010 in a few models (such as CanESM5) and as late as after 2080 in other models (such as GISS-E2-1-G), is larger than that for annual-mean SST. Nevertheless, the estimated ToE of EEP annual-mean rainfall is later than that of annual-mean SST in all models by several decades (Fig. 2b, 3b).

To investigate the cause of the later ToE of annual-mean rainfall, we decompose rainfall change into a thermodynamic component $(-\bar{\omega} \cdot \Delta q)$ due to moisture change, and a dynamic component $(-\Delta\omega \cdot \bar{q})$ due to circulation change based on a simplified moisture budget analysis^{32,33} (see "Decomposition of *annual-mean* SST and rainfall change" in Methods). The result indicates that the weak response of annual-mean rainfall in the ITCZ and SPCZ is caused by an offsetting effect between a positive response of thermodynamic component and a negative response of dynamic component, while the robust positive response of EEP annual-mean rainfall is almost entirely due to the dynamic component—an equatorial and eastward shift in rainfall (Supplementary Fig. 7). As such, the ToE of EEP annual-mean rainfall appears to not be influenced by

the thermodynamic component of rainfall (Fig. 3c–d). Rather, it is almost totally determined by the ToE of dynamic component of rainfall, with the inter-model correlation coefficient between the two being up to 0.98 (Fig. 3e).

The response of EEP dynamic rainfall is controlled by an ascending circulation response, which is driven by a local positive warming response of $T_{\rm r}$ (Supplementary Fig. 7b, contours), suggestive of the "warmer gets wetter" paradigm^{4,32}. The significant (insignificant) inter-model relationship between the response of $-\Delta\omega\cdot \overline{q}$ and $T_{\rm r}$ ($T_{\rm tm}$) in the EEP (Supplementary Fig. 8) further verifies that it is the $T_{\rm r}$, rather than the $T_{\rm tm}$, that plays an important role in the response of EEP dynamic rainfall, contributing to a later ToE of annual-mean rainfall compared with that of the annual-mean SST. Likewise, we would expect the signal of observed annual-mean rainfall, if reliable records are long enough, to emerge later than the signal of observed annual-mean SST.

Time of Emergence of ENSO SST and Rainfall Change Signals

ENSO dominates interannual climate variability in the tropical Pacific, displaying anomalous SST and rainfall over the central to eastern equatorial Pacific^{34,35}. The MEM results of ENSO SST and rainfall in the reference period of 1870-1899, as diagnosed from an empirical orthogonal function (EOF) analysis on interannual SST anomalies in the 30-year period (see "ENSO-related SST and rainfall variability" in Methods), capture the common features of ENSO patterns (Fig. 4a, b), although there are common biases such as an excessive westward extension of ENSO SST and rainfall^{36,37}.

To diagnose **signal** of ENSO SST in response to global warming in each model, we applied EOF analysis to SST anomalies in each 30-year time window moving

forward by one year ending in 1899 to 2099 (recorded as the ending year of the window). The application produces an evolution of grid-point ENSO SST change from that of the reference period over the 1899 to 2099 period. Similarly, the evolution of global warming signal from the reference period is constructed by 30-year running averages of the yearly time series, producing an evolution from 1899-2099, which is then smoothed by fitting a fourth order polynomial. Evolution of grid-point ENSO SST signal is obtained by regressing the evolution of the 30-year running grid-point ENSO SST change onto the evolution of smoothed 30-year running global warming signal (see "Signal, noise and ToE of ENSO SST and rainfall" in Methods).

The map of MEM regression coefficients under the four SSP scenarios all display an enhancement in SST variability, as well as a westward-shift relative to the reference pattern, with a robust inter-model agreement (Fig. 4c; Supplementary Fig. 9a–c), indicating the presence of the signal. The modelled enhanced ENSO SST response is consistent with the observations, although the westward-shifts are hard to detect in the limited historical period in observations (Supplementary Fig. 9d–f). Similar analysis conducted for ENSO rainfall and their MEM responses, on the other hand, displays a consistent enhancement and an eastward-shift relative to the background pattern^{17,18} (Fig. 4d; Supplementary Fig. 9g–i).

Noise of ENSO SST and rainfall in each model is diagnosed from EOF analysis of each running 30-year ENSO SST and rainfall interannual anomalies, increasing by one year, in a 500-year long piControl experiments. The EOF analysis generates 471 realizations of 30-year running grid-point ENSO SST and rainfall for 471 realizations of change from the 1870-1899 reference period for each model.

The ToE of ENSO SST and rainfall change signals is defined as the 30-year

window when the grid-point signal first exceeds to the 99 percentile (1 percentile) value of the noise for the local ENSO SST response to global warming that is positive (negative). The MEM results of times of emergence of ENSO SST and rainfall, calculated by averaging model results only when more than 70% models have local emergent signals before 2099, show that both signals of ENSO SST and rainfall change are confined to the equatorial region, and are not yet detectable (Fig. 4e, f). The MEM ToE of the ENSO SST signal is located to the west of the referenced ENSO SST center (Fig. 4e), while the MEM ToE of the ENSO rainfall signal is located to the east of the referenced ENSO rainfall center (Fig. 4f). Thus, besides the increased amplitude responses to global warming, the pattern shifts of both ENSO SST and rainfall play an important role in their respective ToE.

To confirm, we decompose the response of grid-point ENSO SST and rainfall to global warming into two components: the amplitude response and the structural response. The former depicts the intensity change by assuming that the spatial pattern under global warming is fixed, while the latter indicates shifts in spatial pattern (see "Separation of amplitude and structural changes in ENSO SST and rainfall" in Methods). For ENSO SST, the increased amplitude response and the westward-shifted structural response make comparable contributions to the total signal of ENSO SST (Supplementary Fig. 10a, b). While for ENSO rainfall, the eastward-shifted structural response plays a more important role in the ENSO rainfall response compared with the increased amplitude response (Supplementary Fig. 10c, d).

A comparison between the ToE of ENSO SST and rainfall change signals in the EEP reveals that the modelled ToE of ENSO rainfall signal is generally sooner than that of ENSO SST signal by several decades (Fig. 5), which is opposite to the ToE of annual-mean SST and rainfall change signals. In the MEM, the ENSO SST signal is expected

to emerge under both the SSP585 and SSP370 scenarios in the 30-year time windows ending at 2070 and 2073, respectively, but not under the other two lower scenarios (SSP126 and SSP245) (Fig. 5a), indicative of some sensitivity to emission scenarios; the ToE of ENSO rainfall, however, is projected to be in this century under all the SSP126, SSP245, SSP370 and SSP585 scenarios in the 30-year time windows ending at 2039, 2045, 2042 and 2037, respectively, separated by less than a decade (Fig. 5b), around 30 years earlier than ENSO SST.

Under the SSP585 scenario, the estimated ToE of ENSO rainfall is also sooner than that of ENSO SST for most individual models (Fig. 5c, d; Supplementary Fig. 11). For ENSO SST, 17 out of 23 (around 74%) models show a ToE before the end of the 21st century (Fig. 5c), while for ENSO rainfall, all but one model (INM-CM5-0) show the ToE (Fig. 5d). A large inter-model spread exists in the ToE of both ENSO SST and rainfall, with the inter-model standard deviation up to 50 years (Fig. 5c, d), which, however, does not change our result of a sooner ToE of ENSO rainfall than ENSO SST. Thus, the signal of ENSO-related variability change, when measured by rainfall^{6,18}, is stronger and will emerge sooner as compared to that measured by SST.

Implications for Emergence of Rainfall Signals

Our estimations for ToE of annual-mean rainfall in the EEP based on MEM reveal that they are dependent on the future emission scenarios, with signals emerging as early as before 2040 under the SSP585 scenario; by contrast, annual-mean rainfall is undetectable by the end of this century under the lowest SSP126 scenario (Fig. 3a). This implies that climate mitigation could be effective in preventing significant rainfall shifts in the mean state. However, the estimated MEM ToE of ENSO rainfall are only a few years apart in the different emission scenarios (Fig. 5b). Hence, we would expect to

detect a significant signal of ENSO rainfall change before 2050 even if we follow a strong mitigation pathway such as the SSP126 or SSP245 scenarios. Considering that ENSO rainfall is the main driver of global ENSO teleconnections, via heating of the atmosphere and the propagation of atmospheric waves to both the tropics and extratropics^{38,39}, the emergent ENSO rainfall change signal could trigger wide-ranging impacts on natural and human systems.

Summary and Caveats

Our results that the annual-mean SST signal emerges sooner than the annual-mean rainfall, whereas the ENSO-related rainfall variability signal emerges sooner than the ENSO-related SST variability are robust in most individual models as well as in their aggregation. We note that the estimated ToE could be affected by persistent model biases. For example, the difference between the observed multidecadal enhancement and a modelled long-term weakening in the equatorial Pacific west-minus-east SST gradient affects the ToE of annual-mean rainfall. However, as we have shown, a pattern with a weakened west-minus-east SST gradient should not be excluded in the future real world. Another uncertainty source is a large inter-model difference in the exact ToE, owing to differences either in background noise, climate change signals influenced by the chaotic nature of the climate system^{16,40}, or both.

Despite these caveats, our result of a sooner ToE of annual-mean SST than annual mean rainfall suggests that focus should be placed on the tropical mean SST for detection of mean state change in the tropical Pacific. In addition, our result of a ToE of ENSO rainfall by around 2040, ~30 years sooner than ENSO SST and insensitive to different emission scenarios, highlights the potential risks of extreme events associated with ENSO rainfall change and the associated ENSO teleconnections.

308 Acknowledgements

309	J.Y was supported by the National Natural Science Foundation of China (Grants
310	41690121, 41690120), the Scientific Research Fund of the Second Institute of
311	Oceanography, Ministry of Natural Resources (Grant QNYC2001), and the Innovation
312	Group Project of the Southern Marine Science and Engineering Guangdong Laboratory
313	(Zhuhai) (No. 311021001). A.T. received funding from the Institute for Basic Science
314	(IBS) under IBS-R028-D1.

Methods

315

CMIP6 models, observed datasets, and processing. We use the historical runs for the 316 period 1870–2014, the four tier-one SSP (SSP126, SSP245, SSP370 and SSP585) 317 scenario runs for the period 2015–2099, and the pre-industrial control (piControl) run 318 for the last 500 years from 23 CMIP6 models²⁴. They are ACCESS-CM2, ACCESS-319 ESM1-5, BCC-CSM2-MR, CanESM5, CESM2-WACCM, CNRM-CM6-1-HR, 320 321 CNRM-CM6-1, CNRM-ESM2-1, EC-Earth3-Veg, FGOALS-f3-L, FGOALS-g3, GFDL-ESM4, GISS-E2-1-G, INM-CM4-8, INM-CM5-0, IPSL-CM6A-LR, MIROC-322 323 ES2L, MIROC6, MPI-ESM1-2-HR, MPI-ESM1-2-LR, MRI-ESM2-0, NorESM2-LM, NorESM2-MM. Note that we have only 499 years in model CESM2-WACCM and 300 324 years in model CNRM-CM6-1-HR in piControl run. For each model, we use only one 325 ensemble member run (r1i1p1f1). Monthly outputs are used of surface temperature (ts, 326 which is SST for open ocean), rainfall (pr), surface air specific humidity (huss), and 327 vertical pressure velocity (wap) at 500hPa. All the model outputs are bilinear 328 interpolated into a $2.5^{\circ} \times 2.5^{\circ}$ grid before analyses. 329 To investigate ToE of observed SSTs, we use three different observational SST datasets: 330 the Hadley Center Sea Ice and SST version 1.1 (HadISSTv1) (ref. 41), the National 331 Oceanic and Atmospheric Administration Extended Reconstructed SST version 5 332 (ERSSTv5) (ref. 42), and the Centennial In Situ Observation-Based Estimates of the 333 Variability of SST and Marine Meteorological Variables version 2 (COBEv2) (ref. 43) 334 for the period 1870–2019. 335 We set the first 30-year of chosen time period 1870–1899 as the reference period. All 336 changes under global warming are calculated by removing the associated values in the 337 338 reference period. Annual-mean values are calculated simply by averaging the monthly values from January and December. Interannual anomaly fields are obtained by quadratic de-trending the monthly values during the chosen period and then removing the climatological annual cycle.

Signal, noise, and ToE of *annual-mean* **SST and rainfall.** To estimate the **signal** of modelled annual-mean SST, we calculate the response of annual-mean SST to global warming. The global warming signal is taken as the annual-mean SST change from the reference period of 1870–1899 averaged over the 60°S–60°N domain and then smoothed by fitting a fourth order polynomial²⁸ (Supplementary Fig. 3b), written as $\tilde{T}(t)$, t=1870-2099. Here we choose the average of SST from 60°S to 60°N to remove inconsistencies caused by sea ice in observational SSTs but not in modelled surface temperature (ts). Our conclusions do not change if a different domain, say, 90° S– 90° N, is chosen to compute the global warming signal. The signal of grid-point annual-mean SST, $S_{AM-SST}(x,y,t)$, is obtained by regressing grid-point annual-mean SST change onto the global warming time series $\tilde{T}(t)$:

$$S_{\text{AM-SST}}(x, y, t) = a(x, y) \cdot \tilde{T}(t) + b(x, y) \tag{1}$$

where a is the regression coefficient, representing the response of annual-mean SST to global warming, and b is the intercept.

The **noise** of grid-point annual-mean SST, $N_{\rm AM-SST}(x,y)$, is defined as the interannual standard deviation of annual-mean SST, which is based on the last 500 years of piControl run. In observations, calculation for the signal of grid-point annual-mean SST is the same as those in models except that it is based on the period 1870–2019, while the noise of observational annual-mean SST is obtained by calculating standard deviation of the annual-mean SST after the signal removed. Modelled signal

 $(S_{\text{AM-rainfall}}(x, y, t))$ and noise $(N_{\text{AM-rainfall}}(x, y))$ of annual-mean rainfall are similarly calculated.

The **ToE** of grid-point annual-mean SST is defined as the first year when the grid-point signal-to-noise ratio of annual-mean SST, $S_{\rm AM-SST}/N_{\rm AM-SST}$, is higher (lower) than 1.0 (-1.0) if the local response of annual-mean SST to global warming (a(x,y)) is positive (negative), as in a previous study²⁸. Calculation for the ToE of annual-mean rainfall is similar to that for annual-mean SST. Note that the chosen threshold value of $S_{\rm AM-SST}/N_{\rm AM-SST}$ for a detectable annual-mean signal is somewhat subjective. If a larger threshold, say 2.0 (-2.0), is chosen²⁸, the estimated times of emergence of annual-mean SST and rainfall would be later by around 20–30 years (not shown), but our result of a sooner ToE of annual-mean SST compared with that of annual-mean rainfall does not change.

Decomposition of *annual-mean* SST and rainfall change. The annual-mean SST change from the reference period in each grid point can be decomposed into a tropical-mean SST ($T_{\rm tm}$) change averaged over 20°S to 20°N and relative SST ($T_{\rm r}$) that is the deviation from the tropical-mean SST. The annual-mean rainfall change can be decomposed, from a water vapor budget, into the changes in thermodynamic and dynamic component^{32,33}:

380
$$\Delta P(x, y, t) \sim -\Delta \omega(x, y, t) \cdot \overline{q(x, y)} - \overline{\omega(x, y)} \cdot \Delta q(x, y, t)$$
 (2)

where Δ denotes the change relative to the value in the reference period; the overbar denotes the climatological value in the reference period 1870–1899; q is surface specific humidity and ω is vertical pressure velocity at 500hPa. The term $-\Delta\omega\cdot\overline{q}$ is the dynamic component of rainfall change, which represents the contributions of

atmospheric circulation change, while the term $-\overline{\omega} \cdot \Delta q$ is the thermodynamic component of rainfall change, which represents the contributions of moisture change⁴⁴.

387

388

389

390

391

392

393

394

395

396

397

398

399

400

401

402

403

404

405

406

Signal, noise, and ToE of ENSO SST and rainfall. Empirical orthogonal function (EOF) analysis is used to extract the spatial pattern of ENSO SST in each model and observation in the tropical Pacific (20°S-20°N, 120°E-80°W). For each model, the EOF analysis is performed on interannual anomalies of each 30-year time window moving forward by one year starting from 1870 to 2099, generating an evolution of 30year running variability for time from 1899 to 2099 (recorded as the ending year of each 30-year time window), $EN_{\text{SST}}(x, y, t_{\text{e}})$, $t_{\text{e}} = 1899 - 2099$, and evolution of change of the 1870-1899, **ENSO SST** reference period over $\Delta EN_{\rm SST}(x,y,t_{\rm e}) = EN_{\rm SST}(x,y,t_{\rm e}) - \overline{EN_{\rm SST}(x,y)}$. The EOF outputs are arranged such that the principal components (PCs) are standardized, and the patterns of EOF modes describe variability of the modes. The absolute values of the EOF patterns are taken to ensure they are positive. The first EOF mode in each period defines the ENSO SST, and the ENSO rainfall is defined by regressing grid-point interannual anomalies of rainfall onto the first PC of ENSO SST.

The evolution of the corresponding global warming signal is taken as the 30-year climatological SST change from the reference period, smoothed by fitting a fourth order polynomial, written as $\tilde{T}_{\rm c}(t_{\rm e})$, corresponding to changes in ENSO SST, $\Delta EN_{\rm SST}(x,y,t_{\rm e})$, in each 30-year time window ending from 1899 to 2099.

The evolution of the **signal** of grid-point ENSO SST change, $S_{\text{EN-SST}}(x, y, t_{\text{e}})$, is obtained by regressing grid-point ENSO SST change $\Delta EN_{\text{SST}}(x, y, t_{\text{e}})$ onto the global

407 warming time series of $\tilde{T}_{c}(t_{e})$:

408
$$S_{\text{EN-SST}}(x, y, t_{\text{e}}) = c(x, y) \cdot \tilde{T}_{\text{c}}(t_{\text{e}}) + d(x, y)$$
 (3)

- where c is the regression coefficient, representing the response of ENSO SST to
- 410 global warming, and d is the intercept.
- The same EOF analysis is applied to each 30-year time window moving forward by one
- 412 year for the last 500 years of the piControl run to diagnose **noise**. The application of
- EOF generates 471 realizations of 30-year running grid-point ENSO SST and their
- changes from the reference period of 1870-1899, written as $\Delta EN_{\rm SST}(x,y,t_{\rm e-pi})$, where
- 415 $t_{\text{e-pi}}$ represents each of the 471 30-year time windows in the piControl run. Calculations
- for the modelled signal of ENSO rainfall ($S_{\text{EN-rainfall}}(x, y, t_{\text{e}})$) and the 471 realizations of
- 417 ENSO rainfall changes in the piControl run from the reference period
- 418 $(\Delta EN_{\text{rainfall}}(x, y, t_{\text{e-pi}}))$ are similar to those for ENSO SST.
- The **ToE** of ENSO SST is defined as the first 30-year time window when the signal,
- 420 $S_{\text{EN-SST}}(x,y,t_{\text{e}})$, is higher (lower) than the 99% (1%) value of the noise,
- 421 $\Delta EN_{\rm SST}(x,y,t_{\rm e-pi})$, for grid-point ENSO SST responses to global warming (c in Eq. 3)
- that are positive (negative).
- 423 For observations, calculation of the signal of ENSO SST is the same as for models
- except that it is based on the period 1870–2019. But when calculating the **noise**, we
- first remove the least squares quadratic trend of the monthly SST value for the whole
- period 1870–2019, and the remaining is treated as the unforced data, which is analogous
- to the output in piControl run in models. Then the changes in ENSO SST in each 30-
- 428 year time window moving forward by one year from the remaining unforced data

relative to the reference period of 1870-1899 are calculated to represent the noise. In 429 an 1870–2019 period, we can obtain 121 samples of such change, which are analogous 430 to the 471 samples of $\Delta EN_{\rm SST}(x,y,t_{\rm e-pi})$ in models. The ToE of observational ENSO 431 SST is estimated by making a comparison between the signal of ENSO SST and the 432 433 above 121 samples of ENSO SST change in a similar statistical way as in models. To illustrate, we use one model (EC-Earth3-Veg) and one observational SST 434 (HadISSTv1) and specify a grid-point (0°, 120°W) to give a brief description of how to 435 estimate the ToE of ENSO SST (Supplementary Fig. 12). Both the EC-Earth3-Veg and 436 HadISSTv1 display increased signal of ENSO SST with time for the specified grid-437 438 point (Supplementary Fig. 12a), indicating a positive ENSO SST response to global warming. As such, we choose the $\Delta EN_{SST}(x, y, t_{e-pi})$ value that is higher than the 99-439 percentile value of all the variability samples (471 samples for EC-Earth3-Veg and 121 440 samples for HadISSTv1) as the threshold value for a detectable $S_{\text{EN-SST}}(x,y,t_{\text{e}})$. The 441 threshold value for EC-Earth3-Veg is 0.22 (horizontal black dashed line in 442 443 Supplementary Fig. 12a, b), while that for HadISSTv1 is 0.27 (horizontal red dashed 444 line in Supplementary Fig. 12a, b). The ToE of ENSO SST in the specified grid-point is thus defined as the first 30-year when the $S_{\text{EN-SST}}(x,y,t_{\text{e}})$ exceeds the threshold 445 value. As shown in Supplementary Fig. 12a, the ToE of ENSO SST in the specified 446 grid-point for EC-Earth3-Veg is the 30-year time window ending at year 2021, while 447 that for HadISSTv1 does not appear, given that the associated signal does not exceed 448 449 the corresponding threshold value even in the last 30-year time window (1990–2019). Calculation for the modelled ToE of ENSO rainfall is similar to that for ENSO SST. 450

The estimated times of emergence of ENSO SST and rainfall could be different when

- choosing different threshold values, but the main conclusions, such as a sooner ToE of ENSO rainfall than that of ENSO SST and both the ToE of ENSO SST and rainfall are not yet detectable, do not change when other threshold values, for example, the 95% (5%) or 97.5% (2.5%), are chosen (Supplementary Table. 1).
- Separation of amplitude and structural changes in ENSO SST and rainfall. The changes in ENSO SST in each 30-year time window from 1870 to 2099 relative to the reference period of 1870–1899, $\Delta EN_{\rm SST}(x,y,t_{\rm e})$, are subjected to a "pattern" regression onto ENSO SST pattern in the reference period, $\overline{EN_{\rm SST}(x,y)}$. The linear regression defines the amplitude change in ENSO SST, $\Delta EN_{\rm SST-amp}(x,y,t_{\rm e})$:

461
$$\Delta EN_{\text{SST-amp}}(x, y, t_{\text{e}}) = \alpha(t_{\text{e}}) \cdot \overline{EN_{\text{SST}}(x, y)} + \beta(t_{\text{e}})$$
 (4)

where α is the "pattern" regression coefficient and β is the intercept. And the residual part represents the structural change in ENSO SST, written as $\Delta EN_{\text{SST-str}}(x, y, t_{\text{e}})$:

465
$$\Delta E N_{\text{SST-str}}(x, y, t_{\text{e}}) = \Delta E N_{\text{SST}}(x, y, t_{\text{e}}) - \Delta E N_{\text{SST-amp}}(x, y, t_{\text{e}})$$
 (5).

A separation of ENSO rainfall change is carried out similarly to that of ENSO SST change.

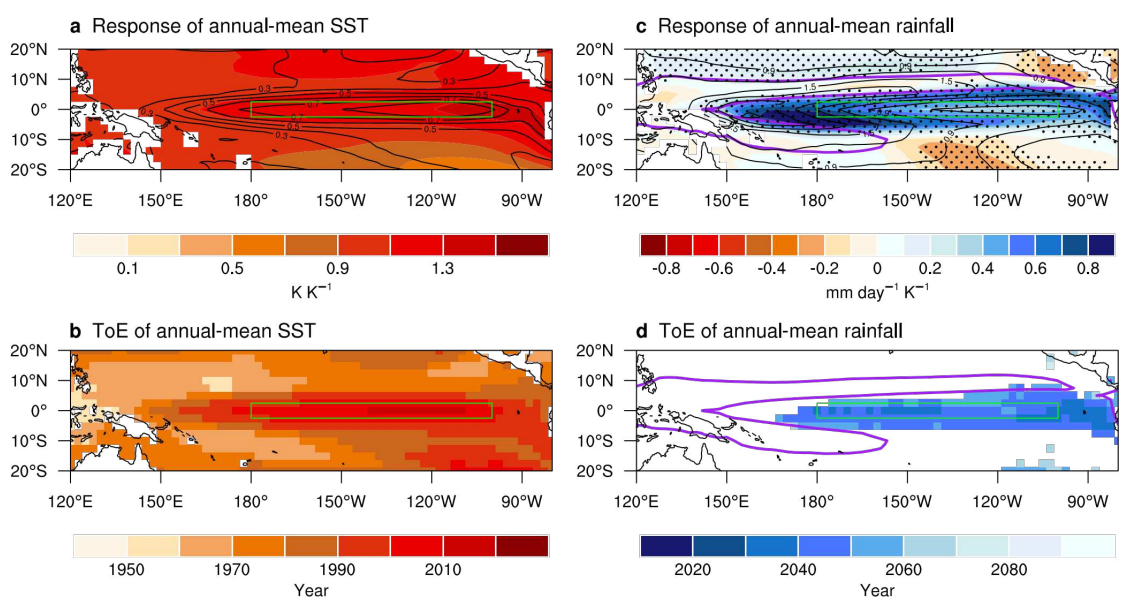
References

- 1 Kosaka, Y. & Xie, S.-P. The tropical Pacific as a key pacemaker of the variable
- 470 rates of global warming. *Nature Geoscience* **9**, 669-673, doi:10.1038/ngeo2770 (2016).
- 471 2 Knutson, T. R. & Manabe, S. Time-Mean Response over the Tropical Pacific to
- 472 Increased CO₂ in a Coupled Ocean-Atmosphere Model. Journal of Climate 8, 2181-
- 473 2199, doi:10.1175/1520-0442(1995)008<2181:TMROTT>2.0.CO;2 (1995).
- 474 3 Vecchi, G. A., Clement, A. & Soden, B. J. Examining the Tropical Pacific's
- 475 Response to Global Warming. Eos, Transactions American Geophysical Union 89, 81-
- 476 83, doi:10.1029/2008EO090002 (2008).
- 477 4 Xie, S.-P. et al. Global Warming Pattern Formation: Sea Surface Temperature and
- 478 Rainfall. *Journal of Climate* **23**, 966-986, doi:10.1175/2009jcli3329.1 (2010).
- 479 5 Ying, J., Huang, P. & Huang, R. Evaluating the formation mechanisms of the
- equatorial Pacific SST warming pattern in CMIP5 models. Advances in Atmospheric
- 481 *Sciences* **33**, 433-441, doi:10.1007/s00376-015-5184-6 (2016).
- 6 Cai, W. et al. ENSO and greenhouse warming. Nature Climate Change 5, 849-859,
- 483 doi:10.1038/nclimate2743 (2015).
- 484 7 Cai, W. et al. Changing El Niño–Southern Oscillation in a warming climate. *Nature*
- 485 Reviews Earth & Environment, doi:10.1038/s43017-021-00199-z (2021).
- 8 Deser, C., Phillips, A. S. & Alexander, M. A. Twentieth century tropical sea surface
- 487 temperature trends revisited. Geophysical Research Letters 37,
- 488 doi:10.1029/2010gl043321 (2010).
- 9 Bordbar, M. H., Martin, T., Latif, M. & Park, W. Role of internal variability in
- recent decadal to multidecadal tropical Pacific climate changes. Geophysical Research
- 491 Letters 44, 4246-4255, doi: https://doi.org/10.1002/2016GL072355 (2017).
- 492 10 Cai, W. et al. Increased variability of eastern Pacific El Niño under greenhouse
- 493 warming. *Nature* **564**, 201-206, doi:10.1038/s41586-018-0776-9 (2018).
- 494 11 Ying, J., Huang, P., Lian, T. & Chen, D. Intermodel Uncertainty in the Change of
- 495 ENSO's Amplitude under Global Warming: Role of the Response of Atmospheric
- 496 Circulation to SST Anomalies. *Journal of Climate* 32, 369-383, doi:10.1175/jcli-d-18-
- 497 0456.1 (2019).
- 498 12 Stevenson, S. L. Significant changes to ENSO strength and impacts in the twenty-
- 499 first century: Results from CMIP5. Geophysical Research Letters 39, L17703,
- 500 doi:10.1029/2012gl052759 (2012).
- Watanabe, M. et al. Uncertainty in the ENSO amplitude change from the past to
- the future. Geophysical Research Letters 39, L20703, doi:10.1029/2012GL053305
- 503 (2012).
- 14 Rashid, H. A., Hirst, A. C. & Marsland, S. J. An atmospheric mechanism for ENSO
- amplitude changes under an abrupt quadrupling of CO2 concentration in CMIP5
- models. Geophysical Research Letters 43, 1687-1694, doi:10.1002/2015GL066768
- 507 (2016).
- 508 15 Zheng, X.-T., Xie, S.-P., Lv, L.-H. & Zhou, Z.-Q. Intermodel Uncertainty in ENSO
- Amplitude Change Tied to Pacific Ocean Warming Pattern. Journal of Climate 29,
- 510 7265-7279, doi:doi:10.1175/JCLI-D-16-0039.1 (2016).

- 511 16 Cai, W. et al. Butterfly effect and a self-modulating El Niño response to global
- warming. *Nature* **585**, 68-73, doi:10.1038/s41586-020-2641-x (2020).
- 17 Power, S., Delage, F., Chung, C., Kociuba, G. & Keay, K. Robust twenty-first-
- century projections of ElNino and related precipitation variability. *Nature* **502**, 541-545,
- 515 doi:10.1038/nature12580 (2013).
- 516 18 Cai, W. et al. Increasing frequency of extreme El Nino events due to greenhouse
- warming. *Nature Climate Change* **4**, 111-116, doi:10.1038/nclimate2100 (2014).
- 518 19 Huang, P. & Xie, S.-P. Mechanisms of change in ENSO-induced tropical Pacific
- rainfall variability in a warming climate. Nature Geoscience 8, 922-926,
- 520 doi:10.1038/ngeo2571 (2015).
- 521 20 Hu, K., Huang, G., Huang, P., Kosaka, Y. & Xie, S.-P. Intensification of El Niño-
- 522 induced atmospheric anomalies under greenhouse warming. Nature Geoscience 14,
- 523 377-382, doi:10.1038/s41561-021-00730-3 (2021).
- 524 21 Yun, K.-S. et al. Increasing ENSO-rainfall variability due to changes in future
- 525 tropical temperature–rainfall relationship. Communications Earth & Environment 2, 43,
- 526 doi:10.1038/s43247-021-00108-8 (2021).
- 527 22 Cai, W. et al. More extreme swings of the South Pacific convergence zone due to
- 528 greenhouse warming. *Nature* **488**, 365-369, doi:10.1038/nature11358 (2012).
- 529 23 Timmermann, A. Detecting the Nonstationary Response of ENSO to Greenhouse
- 530 Warming. Journal of the Atmospheric Sciences **56**, 2313-2325, doi:10.1175/1520-
- 531 0469(1999)056<2313:dtnroe>2.0.co;2 (1999).
- 532 24 Eyring, V. et al. Overview of the Coupled Model Intercomparison Project Phase 6
- 533 (CMIP6) experimental design and organization. Geosci. Model Dev. 9, 1937-1958,
- 534 doi:10.5194/gmd-9-1937-2016 (2016).
- 535 25 Vecchi, G. A. et al. Weakening of tropical Pacific atmospheric circulation due to
- anthropogenic forcing. *Nature* **441**, 73-76, doi:10.1038/nature04744 (2006).
- 537 26 Collins, M. El Niño- or La Niña-like climate change? Climate Dynamics 24, 89-
- 538 104, doi:10.1007/s00382-004-0478-x (2005).
- 539 27 Song, X. & Zhang, G. J. Role of Climate Feedback in El Niño-Like SST Response
- to Global Warming. *Journal of Climate* **27**, 7301-7318, doi:10.1175/jcli-d-14-00072.1
- 541 (2014).
- 542 28 Hawkins, E. & Sutton, R. Time of emergence of climate signals. Geophysical
- 543 Research Letters **39**, L01702, doi:10.1029/2011gl050087 (2012).
- 544 29 Coats, S. & Karnauskas, K. B. Are Simulated and Observed Twentieth Century
- 545 Tropical Pacific Sea Surface Temperature Trends Significant Relative to Internal
- 546 Variability? Geophysical Research Letters 44, 9928-9937,
- 547 doi:https://doi.org/10.1002/2017GL074622 (2017).
- 548 30 Seager, R. et al. Strengthening tropical Pacific zonal sea surface temperature
- gradient consistent with rising greenhouse gases. *Nature Climate Change* **9**, 517-522,
- 550 doi:10.1038/s41558-019-0505-x (2019).
- 31 Watanabe, M., Dufresne, J.-L., Kosaka, Y., Mauritsen, T. & Tatebe, H. Enhanced
- warming constrained by past trends in equatorial Pacific sea surface temperature
- 553 gradient. *Nature Climate Change* **11**, 33-37, doi:10.1038/s41558-020-00933-3 (2020).
- Huang, P. Regional response of annual-mean tropical rainfall to global warming.

- 555 Atmospheric Science Letters 15, 103-109, doi:doi:10.1002/asl2.475 (2014).
- Huang, P., Xie, S.-P., Hu, K., Huang, G. & Huang, R. Patterns of the seasonal
- response of tropical rainfall to global warming. Nature Geoscience 6, 357-361,
- 558 doi:10.1038/ngeo1792 (2013).
- 34 Ropelewski, C. F. & Halpert, M. S. Global and Regional Scale Precipitation
- Patterns Associated with the El Ni?o/Southern Oscillation. Monthly Weather Review
- **115**, 1606-1626, doi:10.1175/1520-0493(1987)115<1606:garspp>2.0.co;2 (1987).
- 562 35 Deser, C. & Wallace, J. M. Large-Scale Atmospheric Circulation Features of Warm
- and Cold Episodes in the Tropical Pacific. Journal of Climate 3, 1254-1281,
- doi:10.1175/1520-0442(1990)003<1254:lsacfo>2.0.co;2 (1990).
- 36 Ham, Y.-G. & Kug, J.-S. Improvement of ENSO Simulation Based on Intermodel
- 566 Diversity. *Journal of Climate* **28**, 998-1015, doi:10.1175/jcli-d-14-00376.1 (2015).
- 37 Jiang, W., Huang, P., Huang, G. & Ying, J. Origins of the Excessive Westward
- Extension of ENSO SST Simulated in CMIP5 and CMIP6 Models. *Journal of Climate*
- **34**, 2839-2851, doi:10.1175/jcli-d-20-0551.1 (2021).
- 570 38 Beverley, J. D., Collins, M., Lambert, F. H. & Chadwick, R. Future Changes to El
- Niño Teleconnections over the North Pacific and North America. *Journal of Climate*
- **34**, doi:10.1175/JCLI-D-20-0877.1 (2021).
- 573 39 Zhou, Z.-Q., Xie, S.-P., Zheng, X.-T., Liu, Q. & Wang, H. Global Warming-
- Induced Changes in El Niño Teleconnections over the North Pacific and North America.
- *Journal of Climate* **27**, 9050-9064, doi:10.1175/jcli-d-14-00254.1 (2014).
- 576 40 Maher, N., Matei, D., Milinski, S. & Marotzke, J. ENSO Change in Climate
- 577 Projections: Forced Response or Internal Variability? *Geophysical Research Letters* 45,
- 578 11,390-311,398, doi:https://doi.org/10.1029/2018GL079764 (2018).
- 579 41 Rayner, N. A. et al. Global analyses of sea surface temperature, sea ice, and night
- 580 marine air temperature since the late nineteenth century. Journal of Geophysical
- 581 Research: Atmospheres **108**, 4407, doi:10.1029/2002JD002670 (2003).
- 582 42 Huang, B. et al. Extended Reconstructed Sea Surface Temperature, Version 5
- 583 (ERSSTv5): Upgrades, Validations, and Intercomparisons. Journal of Climate 30,
- 584 8179-8205, doi:10.1175/jcli-d-16-0836.1 (2017).
- Hirahara, S., Ishii, M. & Fukuda, Y. Centennial-Scale Sea Surface Temperature
- Analysis and Its Uncertainty. Journal of Climate 27, 57-75, doi:10.1175/jcli-d-12-
- 587 00837.1 (2014).

- 588 44 Chou, C., Neelin, J. D., Chen, C.-A. & Tu, J.-Y. Evaluating the "Rich-Get-Richer"
- Mechanism in Tropical Precipitation Change under Global Warming. Journal of
- 590 *Climate* **22**, 1982-2005, doi:10.1175/2008JCLI2471.1 (2009).



593

594

595

596

597

598

599

600

601

602

603

604

605

606

Fig. 1 | MEM response and time of emergence (ToE) of annual-mean SST and rainfall. Shown are based on models under historical forcing and the SSP585 emission scenario. a, Response of annual-mean SST to global warming (see "Signal and noise of annual-mean SST and rainfall" in Methods); b, ToE of annual-mean SST signal; c and d, The same as a and b but for annual-mean rainfall. Contours in a and c denote the MEM noise of SST (units: K, with an interval of 0.1 K) and rainfall (units: mm day⁻¹, with an interval of 0.3 mm day⁻¹), respectively. Stippling in c denotes that more than 70% of models have the same sign. The shaded regions in **b** and **d** denote that more than 70% of models have emergent signals by the year 2099 and are plotted by averaging all the models that show the local ToE by 2099. Purple curves in c and d denote the 7 mm day⁻¹ contour of rainfall climatology in the reference period. The green box in each plot denotes the eastern equatorial Pacific (2.5°S-2.5°N, 180°W-100°W) region. The MEM increasing signal of annual-mean SST has been detected across the whole tropical Pacific, with the latest ToE in the EEP, while that of annual-mean rainfall, which mostly appears in the equatorial Pacific, has yet been detected.

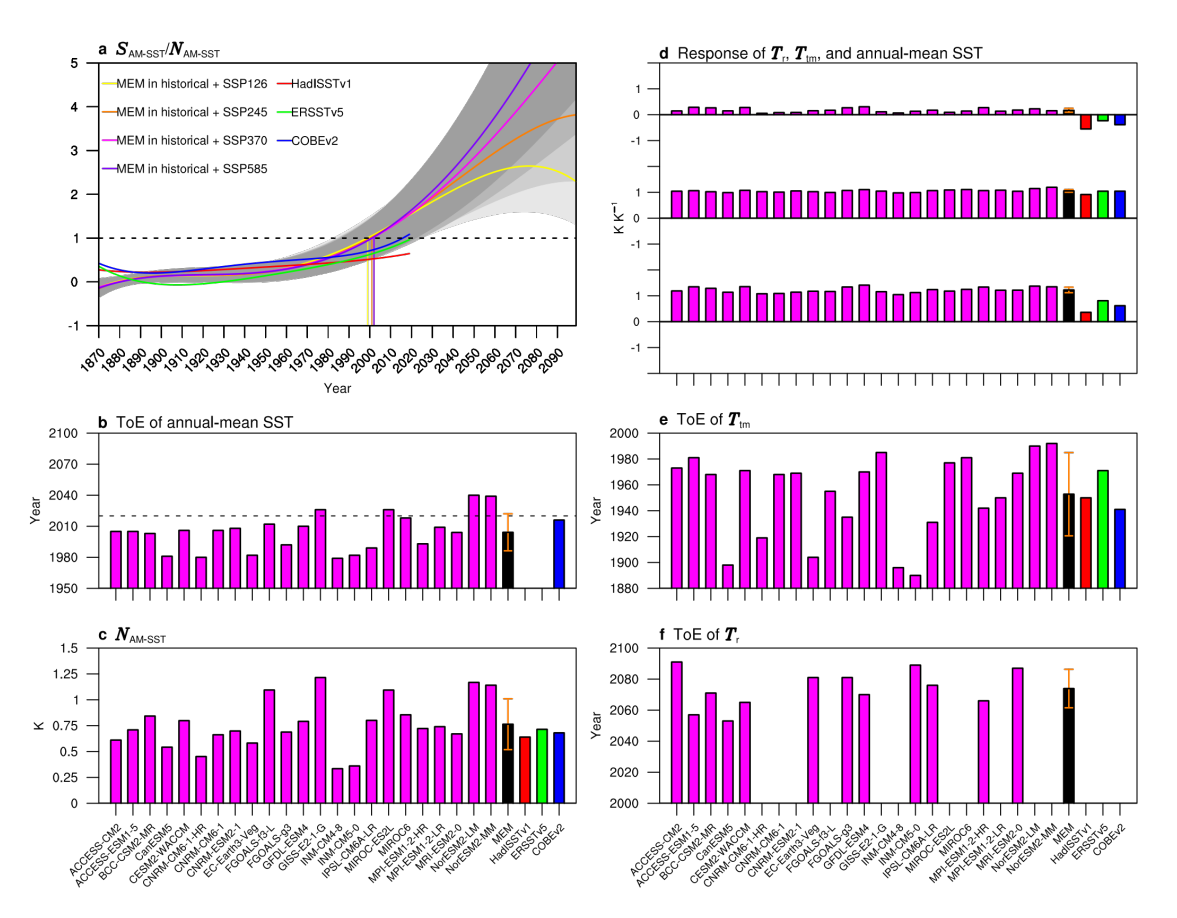


Fig. 2 | ToE of annual-mean SST in the eastern equatorial Pacific. **a**, Signal-to-noise ratio of annual-mean SST in the MEM under historical and four future SSP scenarios and in three observations. The gray shadings denote one inter-model standard deviation, with darker color indicating a higher emission scenario. The vertical solid lines denote the year when the signal-to-noise ratio exceeds 1.0 in different SSP scenarios; **b** and **c**, ToE (**b**), and noise (**c**) of annual-mean SST. The horizontal dashed lines in **b** denotes year 2020; **d**, Responses (from top to bottom) of relative SST (T_r), tropical-mean SST (T_{tm}) and annual-mean SST to global warming (units: K K⁻¹); **e** and **f**, The same as **b**, but for T_{tm} (**e**), and T_r (**f**). Missing bars in **b** and **f** denote the times of emergence for these models (observations) do not appear during 1870–2099 (1870–2019), and the MEM results in **b** and **f** are based on non-missing values. The orange error bars denote one inter-model standard deviation. The modelled shown in **b** and **d**

f are based on historical forcing and the SSP585 emission scenario. The detectable signal of annual-mean SST in the EEP mainly reflects the detectable signal of tropical-mean SST, and the model-observation discrepancy in the ToE of annual-mean SST is caused by the different responses between an observed enhancement and a modelled weakening in the west-minus-east SST gradient.

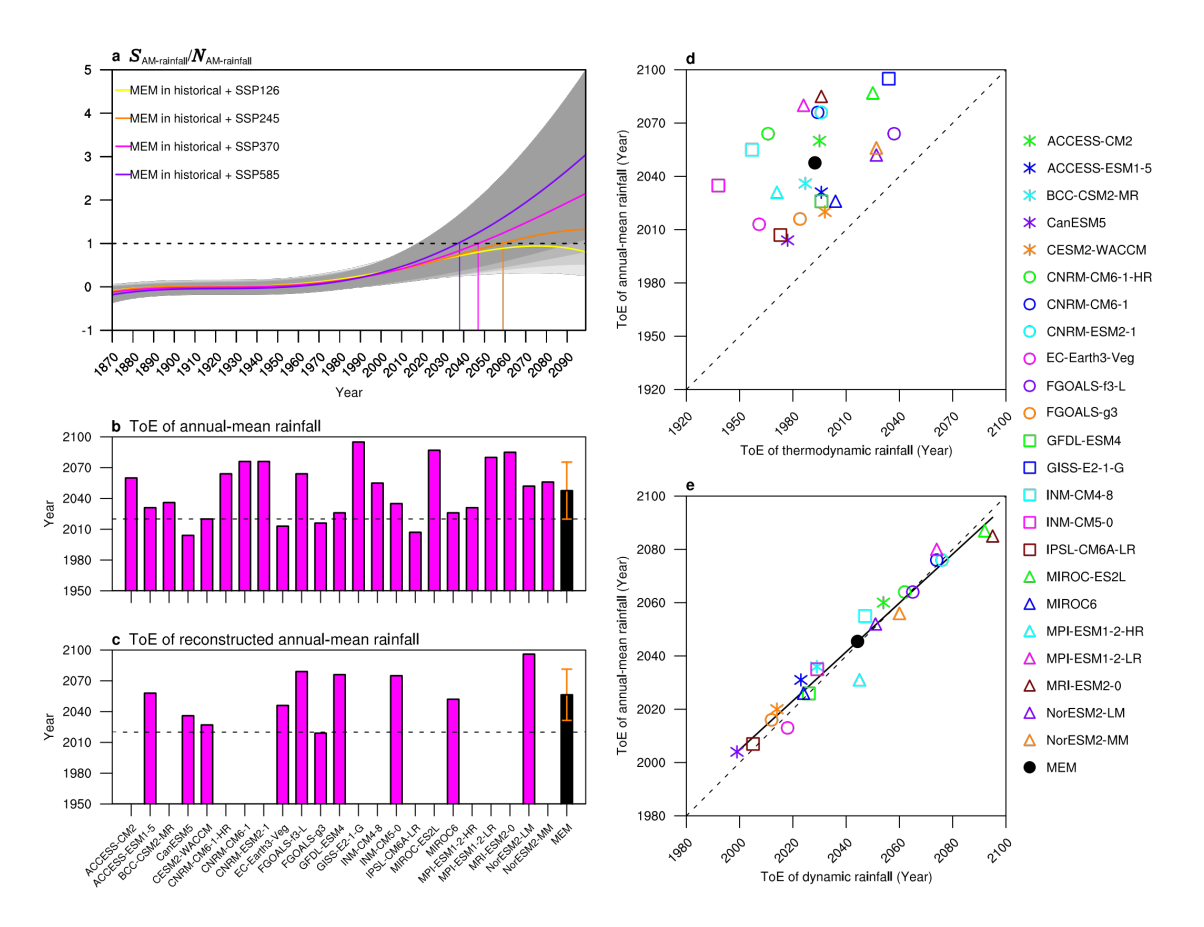


Fig. 3 | ToE of annual-mean rainfall in the eastern equatorial Pacific. a, Signal-to-noise ratio of annual-mean rainfall in the MEM under historical and four future SSP scenarios. The shadings denote one inter-model standard deviation, with darker color indicating a higher emission scenario. The vertical solid lines denote the year when the signal-to-noise ratio exceeds 1.0 in different SSP scenarios; b and c, ToE of annual-mean rainfall (b) and reconstructed annual-mean rainfall (c) (see "Decomposition of annual-mean SST and rainfall change" in Methods). The orange error bars denote one inter-model standard deviation; d and e, Inter-model scatterplots between the ToE for annual-mean rainfall and that for dynamic component (d), and thermodynamic component (e) of annual-mean rainfall. The solid line in e denotes the inter-model linear regression. Missing bars in c and markers in e denote the times of emergence for these models do not appear during 1870–2099, and the MEM result is based on non-missing

values. Shown in **b**–**e** is based on models under historical forcing and the SSP585 emission scenario. The later ToE of annual-mean rainfall than that of annual-mean SST, which appears in around mid-century based on the MEM, is sensitive to emission scenario and is determined by the ToE of its dynamic component.

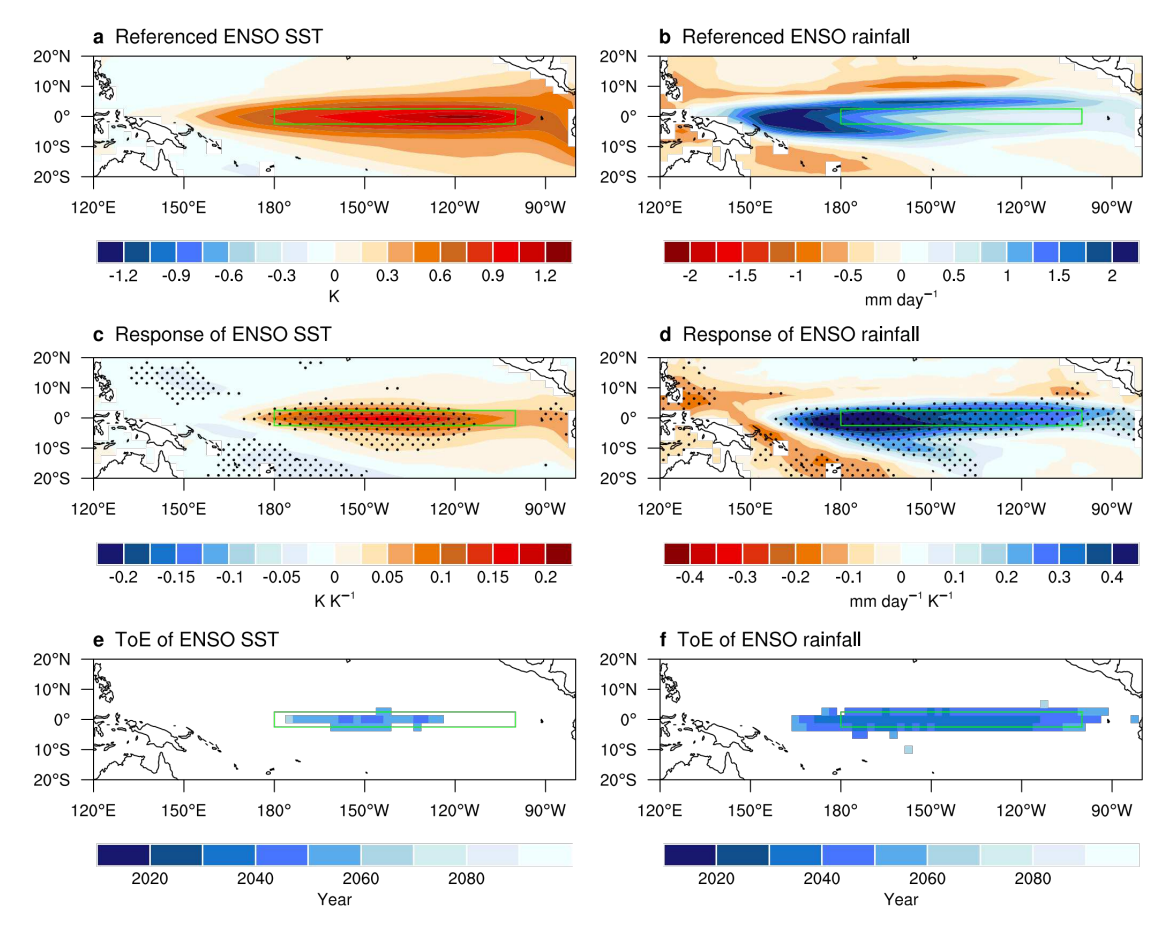
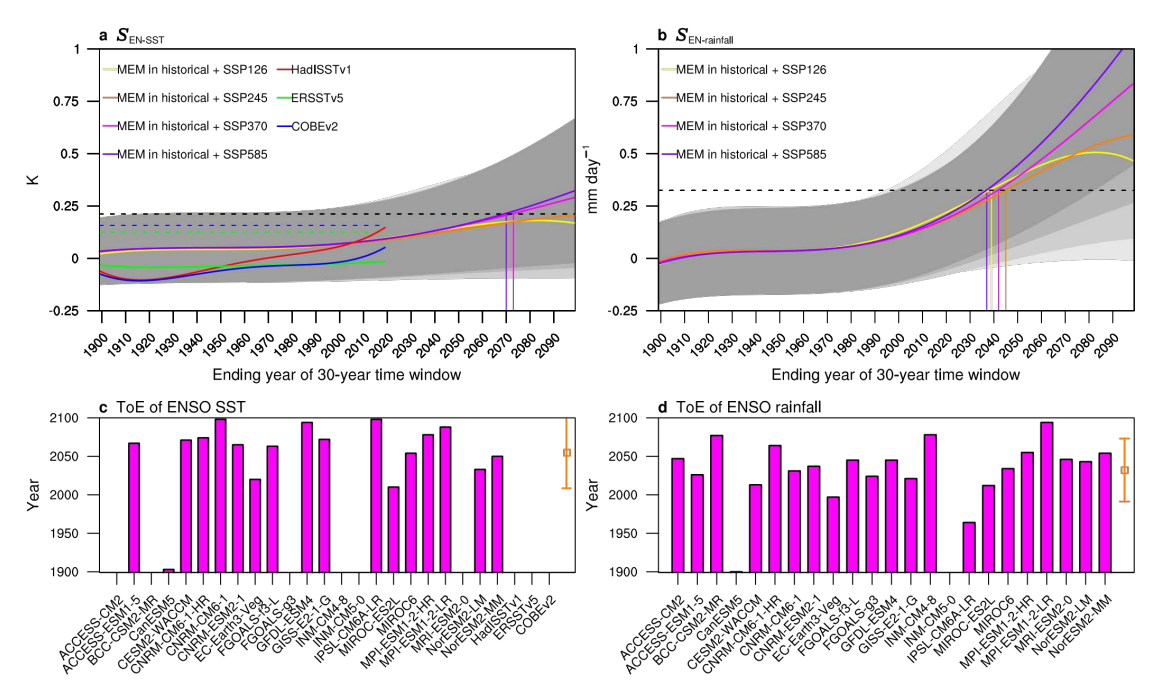


Fig. 4 | **MEM response and ToE of ENSO SST and rainfall. a–b**, Spatial patterns of ENSO SST (**a**) and rainfall (**b**) in the reference period (see "ENSO-related SST and rainfall variability" in Methods); **c** and **d**, Responses of ENSO SST (**c**) and rainfall (**d**) to global warming, which are calculated by regressing the signal of ENSO SST and rainfall onto global warming time series of $\tilde{T}_c(t_e)$, respectively. Stippling denotes where more than 70% of models have the same sign; **e** and **f**, ToE of ENSO SST (**e**) and rainfall (**f**). The shaded regions denote that more than 70% of models have emergent signals, and are plotted by averaging all the models that show the local ToE. Shown in **c**-**f** is based on models under historical forcing and the SSP585 emission scenario. Increasing signals of ENSO SST and rainfall with time, both of which involve not only amplitude change but also pattern shifts, have yet been detected.



656

657

658

659

660

661

662

663

664

665

666

667

668

Fig. 5 | ToE of ENSO SST and rainfall in the eastern equatorial Pacific. a, Signal of ENSO SST in the MEM under historical and four future SSP scenario runs and in three observations. The shading denotes one inter-model standard deviation, with darker color indicating a higher emission scenario. The horizontal black dashed line (0.24) denotes the MEM threshold value for estimating the MEM detectable signal of ENSO SST, while the horizontal colored dashed lines (red is 0.21, green is 0.12 and blue is 0.16) are similar to the black line, but for three observations (see "ToE of ENSO SST and rainfall" in Methods). The vertical solid lines denote the ending year of a 30year time window when the MEM signal of ENSO SST exceeds the defined threshold value; b, The same as a, but for ENSO rainfall only in the MEM. The MEM threshold value for estimating the MEM detectable signal of ENSO rainfall is 0.32 (horizontal dashed line in b); c, ToE of ENSO SST under historical forcing and the SSP585 emission scenario; missing bars denote the times of emergence do not appear before 2099 (2019) for these models (observations). The orange error bars denote one inter-

model standard deviation; **d**, The same as **c**, but for ENSO rainfall. The modelled ToE

of ENSO rainfall is projected to emerge by around 2040±3 based on the MEM

regardless of emission scenarios, around 30 years sooner than that of ENSO SST, which

is with some sensitivity to emission scenarios.

Supplementary Files

This is a list of supplementary files associated with this preprint. Click to download.

• Supplementaryinformation.docx